Research Square

Preprints are preliminary reports that have not undergone peer review.
They should not be considered conclusive, used to inform clinical practice,
or referenced by the media as validated information.

Post-Earthquake Inspection Zoning of Buried Pipelines in Liquefiable Ground Based on Manhole Uplift

[redacted]
University of Science and Technology Beijing
[redacted]
University of Science and Technology Beijing
[redacted]
[redacted]
[redacted]
songbo@ces.ustb.edu.cn

University of Science and Technology Beijing

Research Article

Keywords: Liquefaction, Buried pipeline, Manhole uplift, Axial strain, Inspection zoning, Post-earthquake assessment

Posted Date: October 29th, 2026

DOI: https://doi.org/10.21203/rs.3.rs-11049472/v1

License: This work is licensed under a Creative Commons Attribution 4.0 International License.
Read Full License

Additional Declarations: No competing interests reported.

Post-Earthquake Inspection Zoning of Buried Pipelines in Liquefiable Ground Based on Manhole Uplift

Kewu Zhang[1,2], Jiasheng Jiang[1,2], Qingyun Xu[2,3], and Bo Song[1,2]

[1] Future City College, University of Science and Technology Beijing, Beijing 100083, China

[2] Beijing International Science and Technology Cooperation Base for Seismic Research on Rail Transit Engineering in Strong Earthquake Areas, Beijing 100083, China

[3] China Harbour Engineering Co., Ltd., Beijing 100027, China

Corresponding author: Bo Song; email: songbo@ces.ustb.edu.cn

Abstract

Rapid post-earthquake inspection of buried pipelines in liquefiable ground is difficult because damage is concealed, whereas manhole uplift H can be measured at the surface. This study develops a three-level inspection-zoning method that links this visible field indicator to the internal response of an adjacent buried steel pipe. A coupled FLAC3D model was established for the manhole–pipeline–soil system, including pore-pressure accumulation, degradation of pipe–soil restraint, manhole–soil slip, and load transfer through the manhole–pipeline connection. The model reproduced a field case with approximately 0.50 m uplift; the calculated uplift was 0.553 m, a difference of 10.6%. Twenty-four analyses combined six pulse-like or non-pulse-like records with peak ground accelerations of 0.1–0.4 g. At 0.4 g, pulse-like motions produced a mean uplift of 0.585 m, 2.1 times the non-pulse-like mean of 0.280 m, while the corresponding mean maximum axial strains were 1.073×10^{-3} and 0.856×10^{-3}. Across all cases, H and maximum pipeline axial strain were positively associated (Pearson $r = 0.888$; Spearman $\rho = 0.883$), but strain localization depended additionally on liquefied-zone boundaries and transient deformation compatibility. Accordingly, H is not used to invert actual strain. Instead, case-specific reference boundaries of 0.30 and 0.64 m define routine patrol, review, and priority-inspection zones, with leakage, pressure anomalies, pavement cracking, and joint offset used as escalation criteria. The resulting field chart provides a rapid, observable basis for allocating inspection resources after an earthquake.

Keywords: Liquefaction; Buried pipeline; Manhole uplift; Axial strain; Inspection zoning; Post-earthquake assessment

Acknowledgments

This work was supported by the Science and Technology Research and Development Project of China Harbour Engineering Co., Ltd. (Grant No. 2026-ZGKJ-TDYF-12).

1 Introduction

The total length of urban water-supply, drainage, gas, and heating pipelines in China increased from approximately 1.83 million km in 2014 to approximately 3.78 million km in 2024 [1]. As urban underground networks expand, detailed segment-by-segment inspection after an earthquake requires substantial time and resources. Damage is also concealed below ground, and pipelines in unfavorable sites may uplift, bend, or develop joint abnormalities. Rapidly identifying potentially abnormal segments and establishing an inspection sequence is therefore an immediate need in lifeline emergency response (Fig. 1).

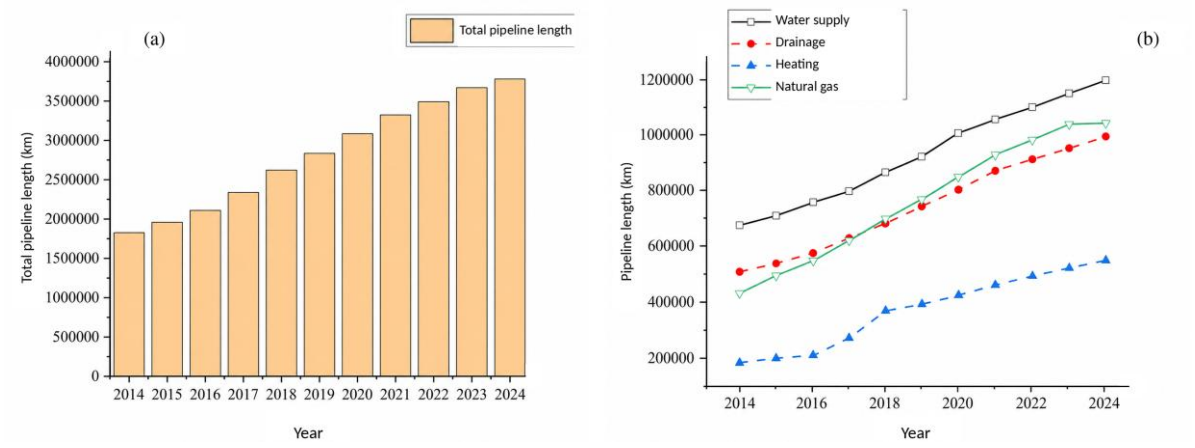


Fig. 1 Changes in urban pipeline length in China: (a) total pipeline length; (b) pipeline length by utility type

The underground utilities in central Weifang, Shandong Province, include multiple systems, densely spaced nodes, and strongly interwoven alignments (Fig. 2). Such networks cannot be screened rapidly by detailed inspection alone. Visible surface evidence can first be used to narrow the search area, after which closed-circuit television inspection, nondestructive testing, pressure testing, or excavation can be assigned preferentially to priority segments.

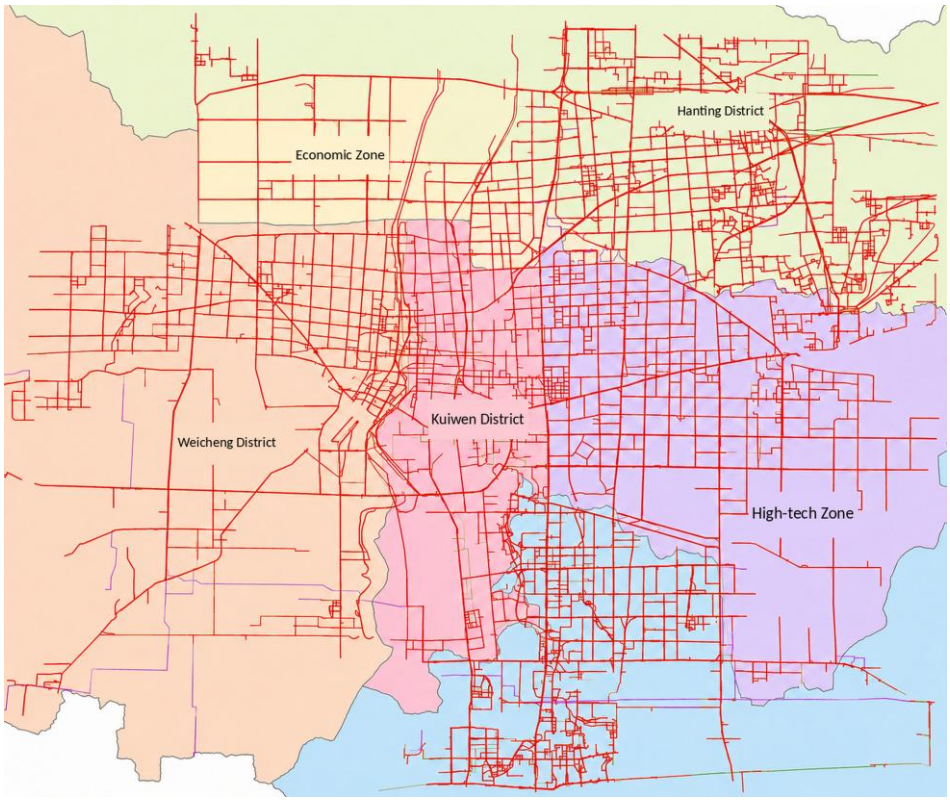


Fig. 2 Schematic distribution of underground pipelines in central Weifang, Shandong Province

Manhole uplift in liquefied ground is conspicuous and readily measurable and commonly accompanies deformation of adjacent roads and pipelines. After the 2011 Tohoku earthquake, approximately 0.50 m of manhole uplift, road heave, and pipeline service damage were reported at multiple sites [2]. During the 2024 Noto Peninsula earthquake, three manholes in Kawai-machi, Wajima City, uplifted by approximately 1.0–1.2 m, with nearby sand boils and road deformation along pipeline alignments [3]. These observations indicate that manhole uplift reflects local liquefaction and backfill deformation and can transfer additional displacement to adjacent pipeline segments through the manhole–pipeline connection (Fig. 3).

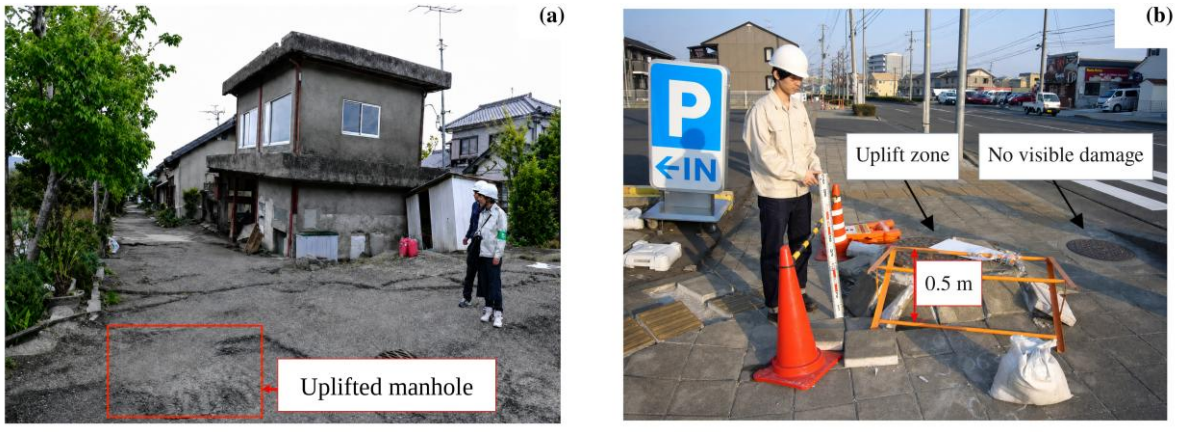


Fig. 3 Manhole uplift in liquefiable ground: (a) observed manhole uplift after the 2007 Niigata-ken Chuetsu-oki earthquake; (b) uplift measurement after the 2011 Tohoku earthquake. Sources: (a) Ref. [4]; (b) Ref. [2]. Reproduced with permission.

The Chinese Seismic Technical Code for Oil and Gas Transmission Pipeline Engineering (GB/T 50470–2017) recommends that pipelines avoid areas with moderate or greater liquefaction potential [5]. Although the code is intended for long-distance oil and gas pipelines, its avoidance principle also demonstrates the adverse effect of liquefaction on buried pipelines. The Standard for Structural Safety Risk Assessment of Urban Municipal Pipelines (T/CECS 1120–2022) further emphasizes the progression from basic data collection through inspection and monitoring to pipeline-unit assessment and risk treatment [6]. The present method does not replace the complete risk assessment prescribed by such standards; rather, it provides an observable field-screening index and an inspection sequence for the information-scarce post-earthquake stage.

Postearthquake surveys established the importance of liquefiable trench backfill and local stratigraphy. Yasuda and Kiku [7] documented uplift of approximately 1,400 sewer manholes during the 2004 Niigataken-Chuetsu earthquake and attributed the response primarily to liquefaction of loose sand backfill; uplift was especially severe in clayey or peaty ground. Kang et al. [8] combined open-cut and level-survey data for 436 uplifted manholes in Nagaoka and showed that shallow groundwater, low standard-penetration resistance, low-permeability clay, and backfill conditions jointly influenced uplift; they also distinguished pipeline uplift caused by manhole traction from uplift caused by pipe buoyancy. Koseki et al. [9] compared damaged and undamaged conditions at 210 sites in Kushiro and found that the two investigated earthquakes damaged approximately 19 km of sewer pipe; thick saturated backfill and an underlying low-permeability peat or liquefiable sand layer amplified damage in wetland and floodplain areas.

Physical modeling clarified the associated deformation mechanisms. Nishio et al. [10] placed a pipeline in a nonliquefiable surface layer above a locally liquefiable sand layer and reproduced the characteristic surface-layer and pipeline motions with simplified mechanical models; prototype-scale calculations indicated that partial liquefaction can generate very large pipeline strains. Ko et al. [11] used actual earthquake records in full-scale shaking-table tests and observed uplift of natural-gas and sewer distribution mains. They further found lower excess-pore-pressure buildup around uplifted pipes than in the free field, particularly above the pipe crown, and cautioned that a simplified anti-uplift model may underestimate the response of large-diameter pipes. Tobita et al. [12] observed liquefied backfill flowing beneath an uplifting manhole in centrifuge tests and identified the overburden-pressure difference between the manhole base and backfill at the same depth as a primary driver; input intensity, trench deformation, groundwater depth, backfill density, and apparent manhole unit weight also affected uplift.

Mechanics-based and numerical studies quantified pipe and soil effects. Lin and Xiong [13] derived an uplift model from virtual work, included nonlinear soil restraint and initial axial force, and used nonlinear incremental finite elements to show that liquefiable-zone length, operational axial force, and initial curvature can amplify pipe uplift. Valizadeh and Ecemis [14] calibrated UBCSAND against shaking-table data for sand–granulated-rubber backfill, examined diameter, burial depth, and acceleration, and used H/D = 2.5 as a case-specific transition between shallow and deep failure mechanisms; they also stated that their uplift equation requires reevaluation for other frequencies and real motions. Chen et al. [15] combined pipe–soil contact with nonlinear soil springs and reported larger uplift and axial stress for greater diameter, liquefied-soil density, and liquefiable-zone length and for smaller wall thickness and burial depth, with stress concentrations near the liquefied–nonliquefied boundary and liquefiable-zone center.

Ground-motion characteristics and operational loads introduce additional variability. Basu and Wijewickreme [16] used a calibrated two-dimensional FLAC–PM4Sand model to examine separately the effects of input-motion amplitude and duration on a steel pipe in saturated loose sand. Mardonov et al. [17] included buoyancy, longitudinal compression induced by temperature and internal pressure, and a three-component Gazli record; under their model conditions, uplift increased with liquefiable-zone length and decreased with pipe diameter. Hu and Pang [18] analyzed 74 underground-structure cases and compared 32 intensity measures using correlation, feasibility, and validity criteria. They identified relative density, intensity measure, critical-layer thickness, and burial depth as dominant factors and found Arias intensity more effective than PGA for characterizing uplift in their cases. These results indicate that PGA is convenient for scaling but does not by itself represent the time-history features governing uplift.

Simplified prediction and mitigation studies have focused mainly on the manhole. Nakao et al. [19] tested a weighted-ring retrofit for existing manholes and found that it reduced uplift risk across different manhole shapes and surrounding groundwater levels. Tobita et al. [20] coupled manhole uplift with trench-backfill settlement through an equal-volume condition, verified the displacement method against 1-g and centrifuge tests, and derived a safety factor that accounts for both quantities. Zhang and Chian [21] incorporated submerged sidewall friction into the uplift balance, obtained safety-factor degradation histories during shaking, and found that the pre-shaking safety factor correlated with final uplift. Lu et al. [22] represented liquefied soil as a highly viscous fluid and derived an analytical uplift model with viscous damping; comparison with multiple experiments gave a mean absolute error of 0.29 m and a general tendency to overpredict centrifuge results.

At the network scale, Jing et al. [23] proposed a regional, multifactor framework for long-distance oil and gas pipelines that integrates real-time monitoring, pipeline susceptibility, ground-motion parameters, and cascading-geohazard prediction through second-level warning, minute-level correction, and hour-level refined assessment. That framework addresses whole-route, multisource coordination. For urban liquefiable sites, however, quantitative evidence remains limited for linking visible uplift of an individual manhole to internal strain in the connected pipe and then to a defensible field inspection priority. Velocity pulses may alter pore-pressure accumulation, uplift history, and localized strain simultaneously, but their influence on the H–εx,max association has not been examined sufficiently.

The manhole and pipeline are mutually constrained through their connection. As liquefaction develops, effective stress decreases and pipe–soil and manhole–soil restraints weaken. The manhole then uplifts under the combined effects of buoyancy and surrounding-soil deformation and, through the manhole–pipeline connection, drives differential vertical displacement in adjacent pipe segments. The manhole vicinity controls the overall displacement amplitude, whereas abrupt deformation compatibility near liquefied–nonliquefied boundaries and manhole-adjacent connections promotes local bending and strain concentration. Consequently, H is an indicator of cumulative deformation, while pipeline strain also depends on the longitudinal displacement gradient, restraint discontinuities, and transient excitation; the two quantities are not in a one-to-one relationship.

On this basis, this study does not use H to directly infer actual pipeline damage; instead, it evaluates the feasibility of H as an indicator for relative post-earthquake inspection ranking. The study makes three main contributions: (1) establishing a local analysis chain from visible manhole uplift to internal pipeline strain and then to inspection zoning; (2) comparing the spatiotemporal evolution of pore pressure, uplift, and axial strain in 24 pulse-like and non-pulse-like cases and evaluating the stability of the H-based association using Pearson, Spearman, and leave-one-record-out checks; and (3) defining routine-patrol, review, and priority-inspection zones while explicitly restricting the numerical boundaries to case-specific reference values. The method is intended for rapid post-earthquake screening and for narrowing the range requiring detailed inspection; it does not replace code-based risk assessment, nondestructive testing, or excavation-based verification.

2 Coupled Manhole–Pipeline–Soil Model and Validation

2.1 Ground-Motion Selection and Processing

Three pulse-like motions (RSN181, RSN723, and RSN1114) and three non-pulse-like motions (RSN160, RSN727, and RSN753) were selected from the PEER NGA-West2 database. Pulse classification followed Shahi

and Baker [24]. Each record was truncated to 30 s at a time step of 0.02 s and scaled to PGA levels of 0.1, 0.2, 0.3, and 0.4 g, where g = 9.81 m/s². The PGA and PGV values in Table 1 are the unscaled record properties and describe record selection rather than analysis intensity. Mw is moment magnitude, Rrup is the shortest distance from the site to the rupture plane, and PGV is peak ground velocity.

Table 1 Selected pulse-like and non-pulse-like ground-motion records

Motion type	RSN	*Mw*	*Rrup* / km	Original PGA / g	Original *PGV* / (cm·s⁻¹)
Pulse-like	181	6.530	1.400	0.449	113.500
Pulse-like	723	6.540	1.000	0.432	134.220
Pulse-like	1114	6.900	3.300	0.348	90.630
Non-pulse-like	160	6.530	2.700	0.777	44.920
Non-pulse-like	727	6.540	5.600	0.837	43.480
Non-pulse-like	753	6.930	3.900	0.645	55.940

Representative acceleration, velocity, and displacement histories and 5%-damped response spectra are compared in Fig. 4. The pulse-like records contain concentrated long-period velocity pulses, whereas energy in the non-pulse-like motions is more distributed in time. Because each group contains only three records, group differences reported below apply to the selected sample and are not extrapolated to a statistical population.

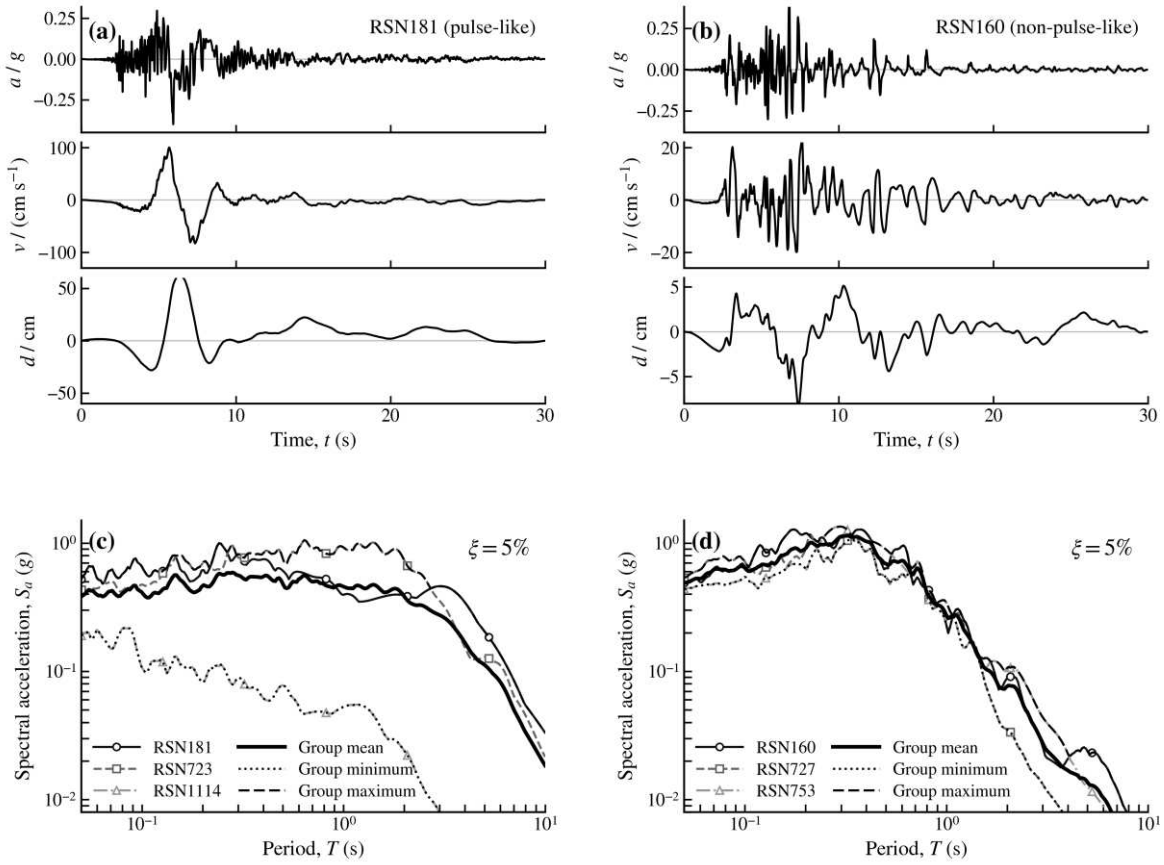


Fig. 4 Comparison of pulse-like and non-pulse-like ground motions: (a) representative pulse-like motion; (b) representative non-pulse-like motion; (c) response spectra of pulse-like motions; (d) response spectra of non-pulse-like motions

2.2 Coupled Numerical Model

The model was 110 m long, 20 m wide, and 9 m high. A 7-m-thick soil layer overlies 2 m of bedrock; the central liquefiable zone is 50 m long, and the two nonliquefiable zones are each 30 m long. The pipeline has an outside diameter D = 0.8 m and was represented by linear-elastic Q235 steel shell elements; the manhole and soil were represented by solid zones. Sand, clay, and bedrock used the Finn, Mohr–Coulomb, and elastic models, respectively (Figs. 5 and 6; Tables 2 and 3).

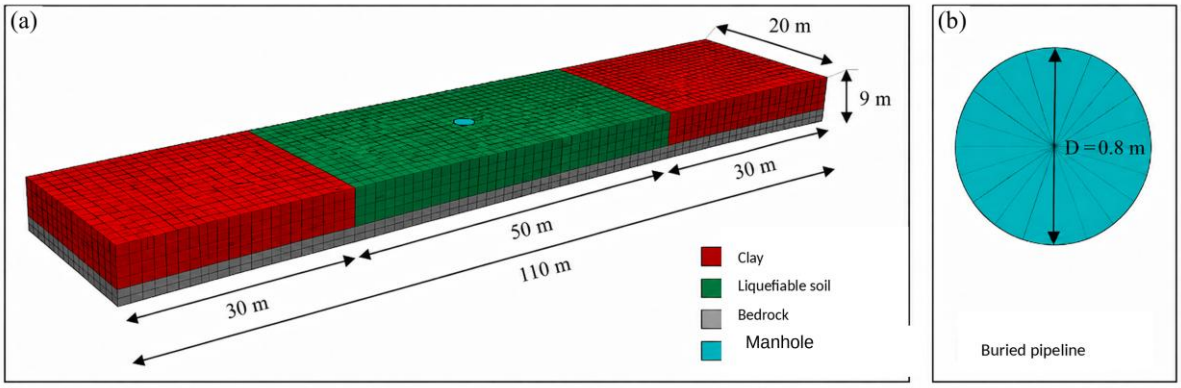


Fig. 5 Numerical finite-difference model: (a) three-dimensional model; (b) pipeline cross section

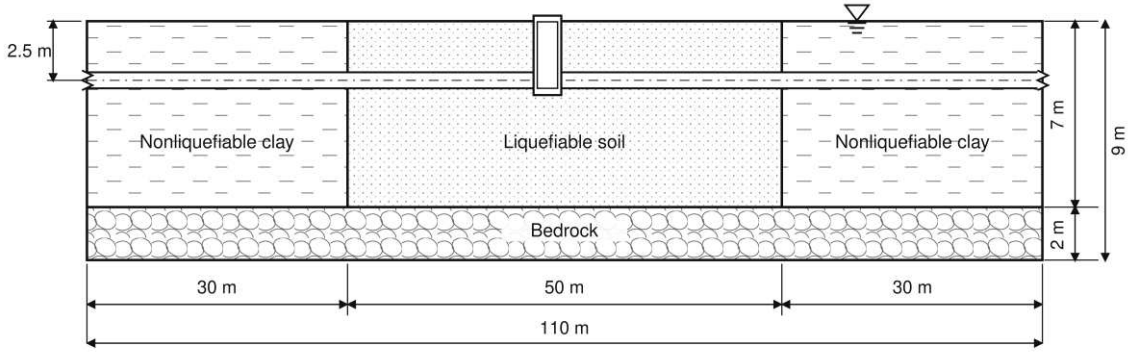


Fig. 6 Geometric dimensions of the numerical model

Table 2 Constitutive parameters of manhole and pipeline materials

Material	Density / (kg·m⁻³)	Elastic modulus / MPa	Poisson's ratio	Yield strain
Q235 steel	7850	2.100×10^5	0.300	1.120×10^{-3}
C30 concrete	2500	3.000×10^4	0.200	—
HRB400 reinforcement	7850	2.100×10^5	0.300	—

Table 3 Soil and bedrock material parameters

Material	Density / (kg·m⁻³)	*K* / MPa	*G* / MPa	Cohesion / kPa	Friction angle / °	Model
Bedrock	2700	1500	1000	—	—	Elastic
Clay	2100	53.500	32.800	32.800	15.400	Mohr–Coulomb
Sand	2050	23.800	7.350	0	32	Finn

The Q235 reference yield strain calculated from the material properties is 1.12×10^{-3} and is used only as a potential-yielding screening line. The linear-elastic pipe model maintains comparability among cases but does not reproduce postyield plasticity, local buckling, or connection failure. Exceeding the line therefore does not constitute a code-based capacity check or deterministic damage diagnosis.

For computational efficiency, the actual circular reinforced-concrete manhole was idealized as a 1.6 m × 1.6 m square solid, 3.2 m high. The idealization preserved the external dimensions, burial depth, approximate global stiffness, and manhole–pipeline connection and is suitable for evaluating overall uplift and its traction on adjacent pipe segments. Wall cracking, ring details, and local connection stresses are outside the scope of the model.

The sand Finn model used the Byrne formulation. Coefficients C_1, C_2, and C_3, which represent the volumetric-strain increment amplitude, cyclic decay, and correction term, were 0.749, 0.534, and 0. Subsequent free-field pore-pressure and displacement histories were used to check the temporal consistency of pore-pressure accumulation, effective-stress reduction, and uplift.

2.3 Manhole–Pipeline–Soil Interaction and Liquefaction Weakening

Structural link elements represented pipe–soil interaction in FLAC3D. Shear-yield springs were assigned in the axial and tangential directions, and normal-yield springs were assigned radially, with parameters calculated according to GB/T 50470–2017 [5]. In Table 4, kx and ky are axial and tangential shear-spring stiffnesses; kz,u and kz,l are the upper- and lower-half radial spring stiffnesses; kn and ks are normal and shear stiffnesses of the manhole–soil interface; k is the manhole–pipeline connection stiffness; and φ, c, and ft are interface friction angle, cohesion, and tensile strength.

Table 4 Manhole–pipeline–soil interaction parameters

Interaction	Parameter	Value	Description
Pipe–soil link	$kx = ky$	9.000×10^6 N·m^{-1}	Axial and tangential shear-yield springs
Pipe–soil link	*kz,u*; *kz,l*	2.880×10^6; 1.480×10^7 N·m^{-1}	Upper- and lower-half radial normal-yield springs
Pipeline–manhole link	*k*	2.000×10^9 N·m^{-1}	High-stiffness connection
Manhole–soil interface	*kn*; *ks*	2.000×10^8; 5.000×10^7 Pa·m^{-1}	Normal and shear interface stiffnesses
Manhole–soil interface	φ; c; *ft*	5°; 0; 0	Friction angle, cohesion, and tensile strength

Pipe–soil spring stiffness decreased continuously as pore-pressure ratio increased. A zone-interface element represented manhole–soil slip and contact weakening, and a high-stiffness link transferred the global constraint between manhole and pipeline. The normal interface stiffness was determined from Eq. (1), and the shear

stiffness was one-quarter of the normal stiffness while also accounting for liquefaction weakening and relative slip.

$$k_n = 10\, max[\frac{K + 4G/3}{\Delta z_{min}}] (1)$$

In Eq. (1), K and G are the bulk and shear moduli of soil adjacent to the interface, in Pa, and Δzmin is the minimum zone dimension normal to the interface, in m. Except at the manhole–pipeline connection, pipe–soil and manhole–soil stiffnesses decreased with pore-pressure ratio; at full liquefaction, the minimum was 1/1000 of the initial stiffness [25].

2.4 Boundary Conditions and Model Validation

During initial stress and seepage equilibrium, the base was fixed, normal displacement was constrained on the side boundaries, and the ground surface was free. During dynamic analysis, a viscous base boundary absorbed incident and reflected waves, and free-field side boundaries represented a semi-infinite site. Motions were input at the base with local damping coefficient 0.26. Gravity stress and pore pressure were equilibrated before each dynamic analysis, and all boundary and damping settings were identical among cases.

The model was validated against an approximately 0.50-m manhole-uplift case from the 2011 Tohoku earthquake [2]. The calculated uplift was 0.553 m, differing by 10.6%, and the global manhole heave and surrounding deformation pattern were consistent with the field evidence (Fig. 7). The comparison supports use of the model for relative comparisons of global uplift and adjacent-pipe response. Because synchronous motion, local soil parameters, and pipeline strain were unavailable for the field case, the validation does not prove a unique local-strain prediction; subsequent strains are used for relative comparisons among cases.

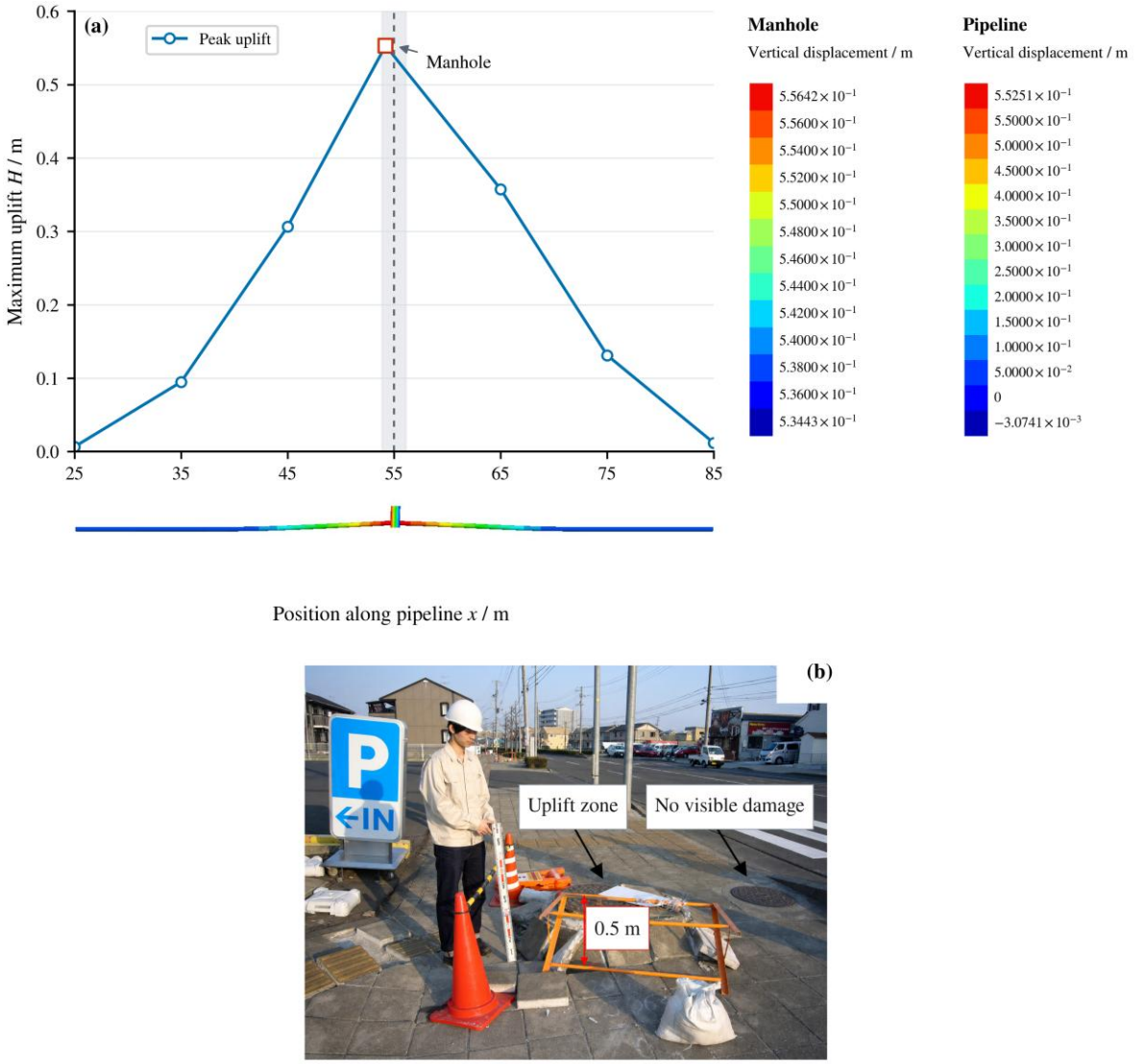


Fig. 7 Comparison between the validation simulation and observed damage: (a) simulated liquefaction-induced manhole uplift; (b) observed manhole uplift after the 2011 Tohoku earthquake. Source: (b) Ref. [2]. Reproduced with permission.

3 Results and Discussion

Responses under the three pulse-like and three non-pulse-like motions were first compared at PGA = 0.4 g and then extended to PGA = 0.1–0.4 g. The analysis focuses on the response chain from pore-pressure development and restraint weakening to manhole uplift and differential pipeline deformation. To avoid ambiguity in the response indices, H denotes the stable postshaking manhole-uplift plateau, whereas $\varepsilon_{x,max}$ is the largest absolute axial strain over the pipeline and the entire analysis duration. The two quantities represent visible cumulative displacement and a localized peak response, respectively.

3.1 Manhole Uplift and Pipeline Strain at PGA = 0.4 g

The pore-pressure ratio in the liquefiable layer increased rapidly under all six records and then fluctuated or approached a stable level (Fig. 8(a–f)), indicating early loss of effective stress. Growth was more concentrated and fluctuated more strongly in the pulse-like group, whereas most non-pulse-like responses stabilized after the initial increase. Pore-pressure accumulation weakened manhole–soil and pipe–soil restraint and enabled uplift, but final displacement also depended on the velocity pulse, effective duration, and system restraint.

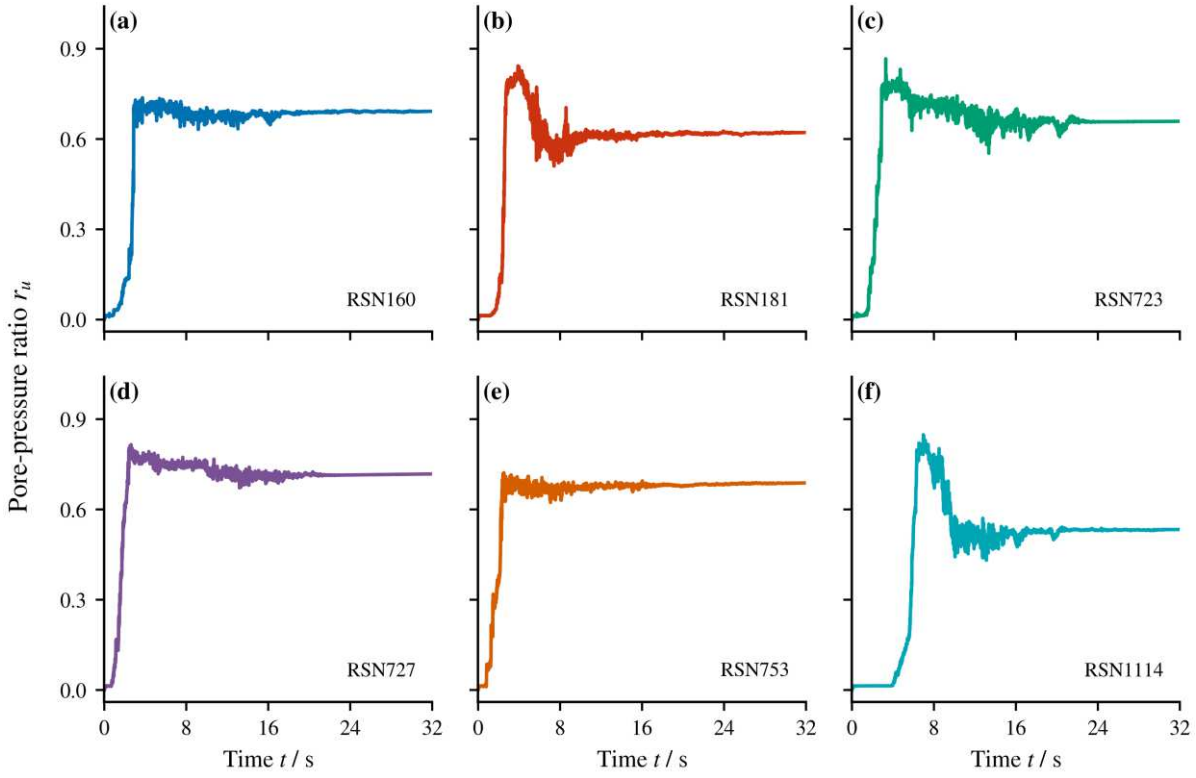


Fig. 8 Time histories of pore-pressure ratio under different ground-motion records: (a) RSN160; (b) RSN181; (c) RSN723; (d) RSN727; (e) RSN753; (f) RSN1114

In Fig. 9(a), ru,max is maximum pore-pressure ratio; tru50 and tru70 are the times at which the ratio reached 0.5ru,max and 0.7; and t0, t50, and t95 are the times at which manhole uplift reached 5%, 50%, and 95% of final uplift Hf. In general, tru70 preceded t0, showing that substantial pore-pressure accumulation and restraint degradation occurred before rapid uplift. Figure 9(b) shows that differences among records were concentrated in the accumulation and stabilization stages. For RSN723, Δt3, from uplift initiation to 50% of final uplift, was approximately 6.17 s; RSN753 reached t95 at approximately 13.86 s and stabilized comparatively early.

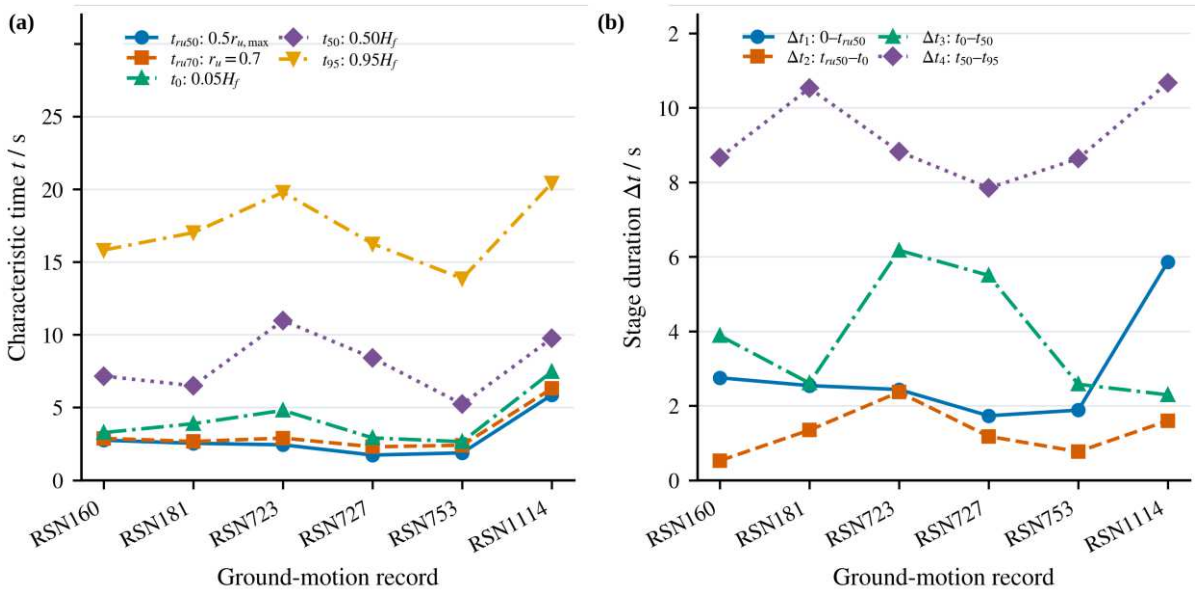


Fig. 9 Characteristic times of the liquefaction-uplift process under pulse-like and non-pulse-like ground motions: (a) characteristic times; (b) stage durations

Maximum uplift along the pipeline peaked at the manhole and decreased toward both sides (Fig. 10), reflecting traction of adjacent pipe segments. At PGA = 0.4 g, H values for RSN160, RSN181, RSN723, RSN727, RSN753, and RSN1114 were 0.281, 0.544, 0.639, 0.305, 0.255, and 0.572 m. The pulse-like mean was 0.585 m, 2.1 times the non-pulse-like mean of 0.280 m. The longitudinal uplift gradient is also important: the manhole controls global amplitude, while differential movement propagated toward liquefied–nonliquefied transitions establishes the condition for local strain concentration.

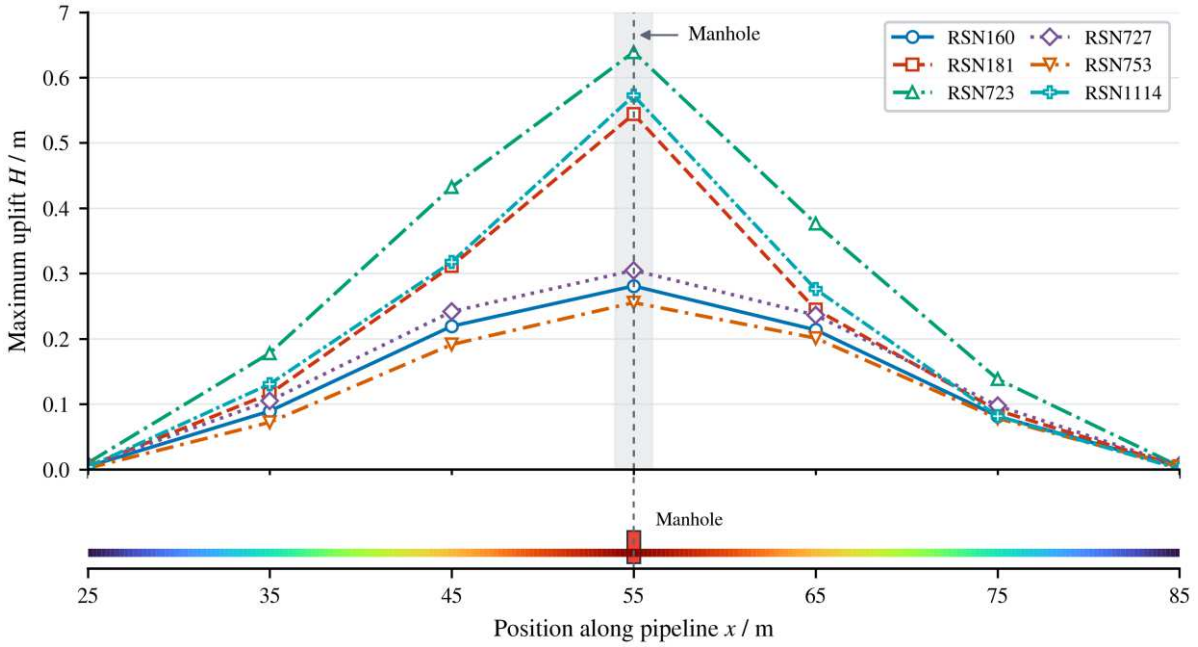


Fig. 10 Distributions of maximum uplift displacement along the pipeline under different ground-motion records

All uplift histories passed through slow development, rapid accumulation, and stabilization (Fig. 11). RSN181 increased rapidly early; RSN723 started later but accumulated through the middle and late stages and reached the largest value. Uplift is therefore a cumulative system response governed jointly by pore pressure, velocity pulse, effective duration, and manhole–pipeline restraint rather than by a single instantaneous acceleration peak.

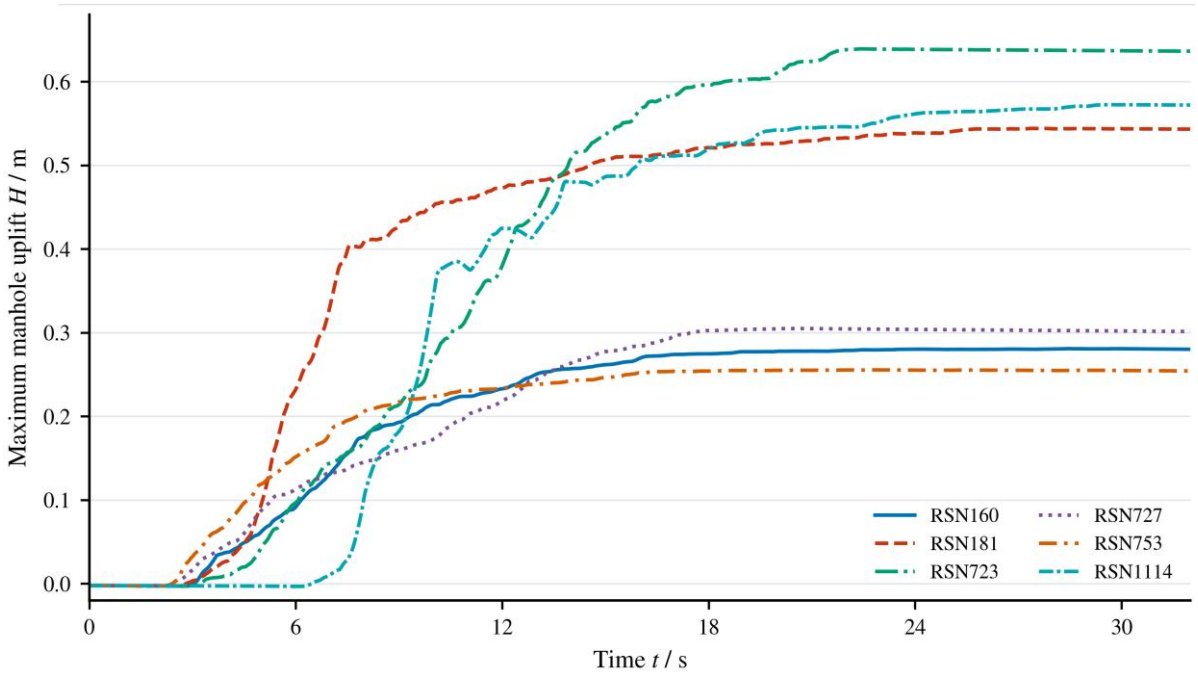


Fig. 11 Time histories of maximum manhole uplift under different ground-motion records

Locations of maximum axial strain did not coincide completely with the maximum-uplift location (Fig. 12). At PGA = 0.4 g, maximum strains for RSN160, RSN181, RSN723, RSN727, RSN753, and RSN1114 were 0.917 × 10^{-3}, 0.976 × 10^{-3}, 1.206 × 10^{-3}, 0.858 × 10^{-3}, 0.793 × 10^{-3}, and 1.036 × 10^{-3}. Only RSN723 exceeded the Q235 reference strain of 1.12 × 10^{-3}. Larger values generally occurred near liquefied–nonliquefied boundaries or manhole-adjacent connections, indicating control by differential displacement, local bending, and restraint discontinuity. Peak-location shifts in RSN181, RSN723, and RSN1114 are consistent with asymmetric uplift and local rotation.

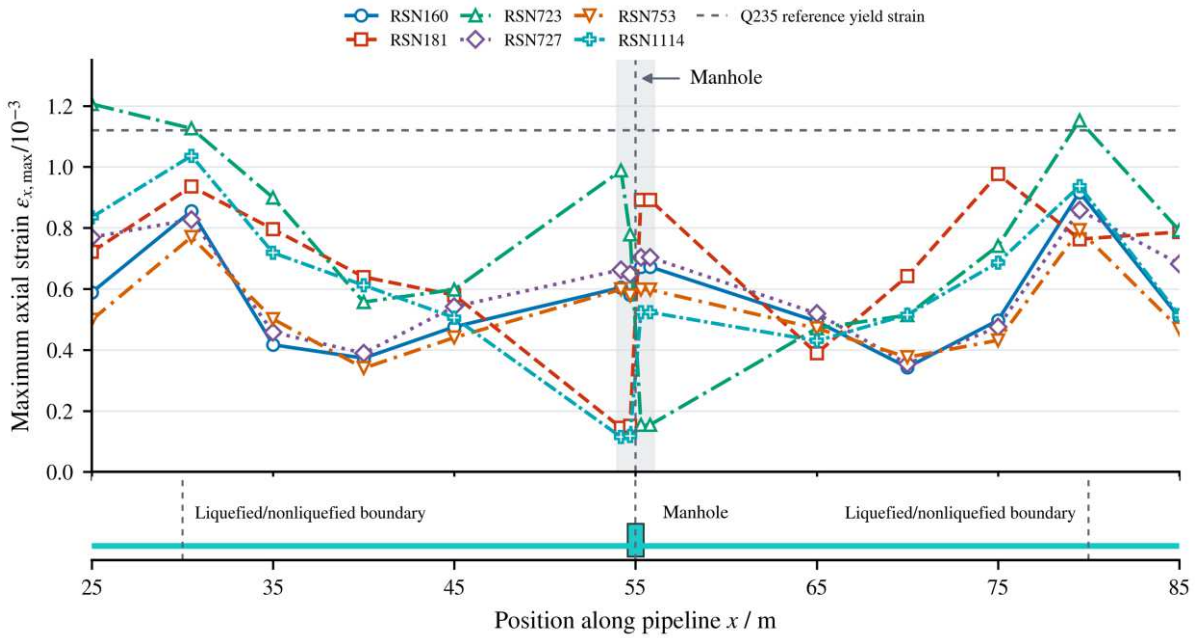


Fig. 12 Distributions of maximum axial strain along the pipeline under different ground-motion records

Maximum axial-strain histories show pronounced dynamic fluctuations, with peaks mainly during rapid pore-pressure growth and rapid uplift (Fig. 13(a–f)). Across the six records, εx,max ranged from 0.793 × 10^{-3} to 1.206 × 10^{-3}; pulse-like and non-pulse-like means were 1.073 × 10^{-3} and 0.856 × 10^{-3}. Unlike cumulative H, axial strain is sensitive to local deformation gradients and transient input, which explains its sign changes and record-to-record scatter and supports using H for ranking rather than direct inversion of εx,max.

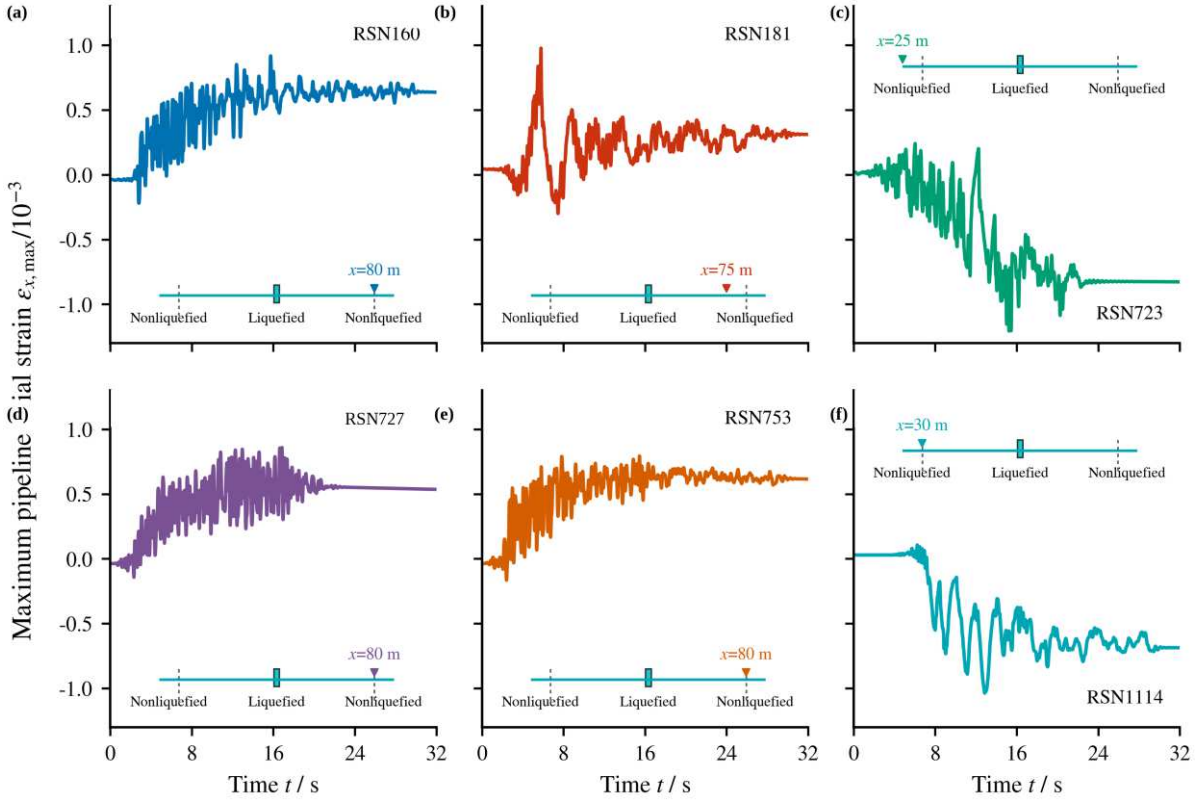


Fig. 13 Time histories of maximum pipeline axial strain under different ground-motion records and corresponding peak locations: (a) RSN160; (b) RSN181; (c) RSN723; (d) RSN727; (e) RSN753; (f) RSN1114

3.2 Effect of PGA Level

Maximum manhole uplift generally increased with PGA (Fig. 14(a,b)). As PGA increased from 0.1 to 0.4 g, pulse-like and non-pulse-like group means increased from 0.170 to 0.585 m and from 0.085 to 0.280 m. H increased in all 18 adjacent-PGA comparisons for the six records. Within the selected sample, the pulse-like mean exceeded the non-pulse-like mean at every PGA, and the absolute difference generally increased with intensity.

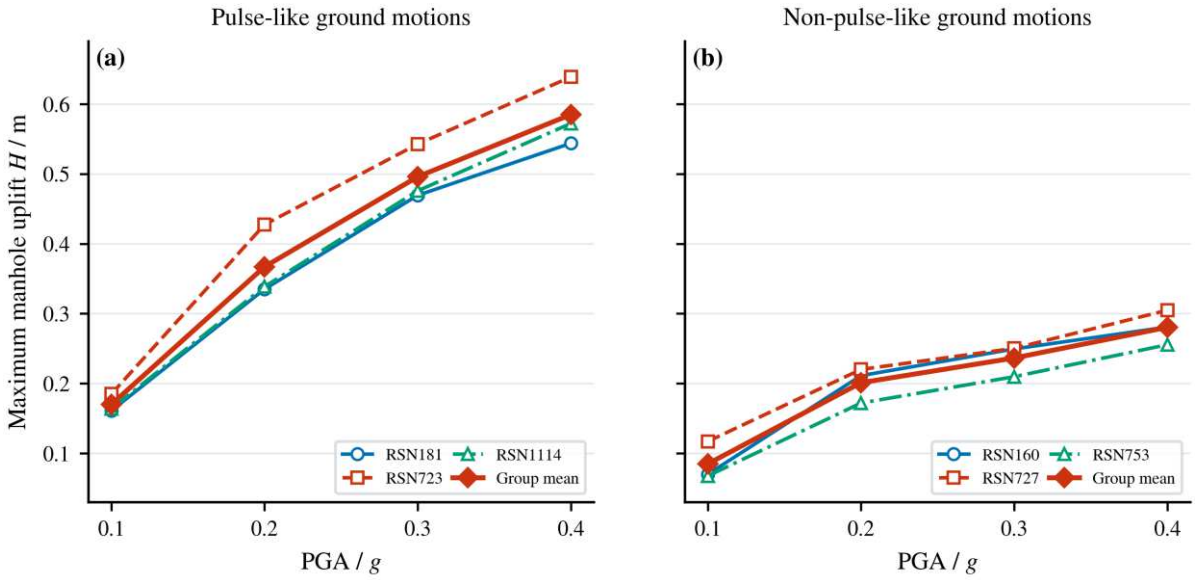


Fig. 14 Maximum manhole uplift and group means at different PGA levels: (a) pulse-like ground motions; (b) non-pulse-like ground motions

Maximum pipeline axial strain also increased in all 18 adjacent-PGA comparisons (Fig. 15(a,b)), but growth differed among records and scatter about the group means was greater than for H. Strain depends on cumulative uplift together with transient input, local restraint, longitudinal deformation gradient, and response phase. H is therefore more suitable as an externally observable ranking index than as a unique determinant of actual strain (Table 5).

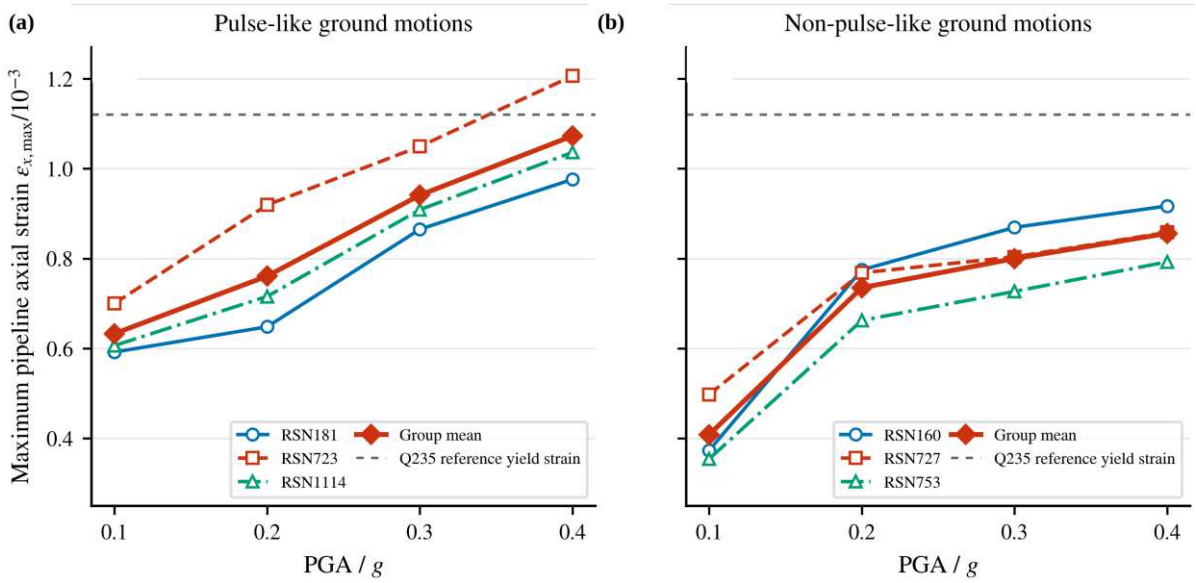


Fig. 15 Maximum pipeline axial strain and group means at different PGA levels: (a) pulse-like ground motions; (b) non-pulse-like ground motions

Table 5 Maximum manhole uplift and maximum pipeline axial strain

RSN	Motion type	PGA / g	H / m	$\varepsilon x,max$ / 10^{-3}
181	Pulse-like	0.100	0.161	0.592
181	Pulse-like	0.200	0.335	0.648
181	Pulse-like	0.300	0.469	0.865
181	Pulse-like	0.400	0.544	0.976
723	Pulse-like	0.100	0.185	0.700
723	Pulse-like	0.200	0.427	0.919
723	Pulse-like	0.300	0.543	1.049
723	Pulse-like	0.400	0.639	1.206
1114	Pulse-like	0.100	0.164	0.607
1114	Pulse-like	0.200	0.339	0.716
1114	Pulse-like	0.300	0.476	0.909
1114	Pulse-like	0.400	0.572	1.036
160	Non-pulse-like	0.100	0.070	0.373
160	Non-pulse-like	0.200	0.211	0.775
160	Non-pulse-like	0.300	0.249	0.869
160	Non-pulse-like	0.400	0.281	0.917
727	Non-pulse-like	0.100	0.117	0.498
727	Non-pulse-like	0.200	0.220	0.768
727	Non-pulse-like	0.300	0.250	0.804
727	Non-pulse-like	0.400	0.305	0.858
753	Non-pulse-like	0.100	0.068	0.354
753	Non-pulse-like	0.200	0.172	0.662
753	Non-pulse-like	0.300	0.210	0.727
753	Non-pulse-like	0.400	0.255	0.793

The pulse-like-to-non-pulse-like mean uplift ratio ηH ranged from 1.8 to 2.1 over PGA = 0.1–0.4 g, while the corresponding strain ratio ηε ranged from 1.0 to 1.6 (Table 6). At PGA = 0.2 g, for example, ηH = 1.826 but ηε = 1.035; a large uplift difference did not imply an equal strain difference. The relatively compact range of ηH and greater dispersion of ηε indicate that velocity pulses amplify cumulative manhole uplift more consistently than local strain. Because H stabilizes late in the histories and is readily observable, it is preferred for initial inspection ranking.

Table 6 Amplification factors of pulse-like ground motions

PGA / g	Pulse mean H / m	Non-pulse mean H / m	ηH	Pulse mean $\varepsilon x,max$ / 10^{-3}	Non-pulse mean $\varepsilon x,max$ / 10^{-3}	$\eta\varepsilon$
0.100	0.170	0.085	2.000	0.633	0.408	1.553
0.200	0.367	0.201	1.826	0.761	0.735	1.035
0.300	0.496	0.236	2.102	0.941	0.800	1.176
0.400	0.585	0.280	2.089	1.073	0.856	1.254

Note: ηH and ηε are ratios of the pulse-like to non-pulse-like group means.

4 Post-Earthquake Inspection Zoning Based on Manhole Uplift

4.1 Quantitative Association Between Uplift and Axial Strain

Fig. 16 summarizes H and εx,max for all 24 cases. Across the full set, the Pearson coefficient was r = 0.888, the Spearman rank coefficient was ρ = 0.883, and the descriptive linear-fit coefficient was R^2 = 0.789. The overall relation was $\varepsilon x,max/10^{-3}$ = 1.108H + 0.441. Pulse-like and non-pulse-like subgroup R^2 values were 0.893 and 0.954, and their descriptive relations were $\varepsilon x,max/10^{-3}$ = 1.123H + 0.398 and $\varepsilon x,max/10^{-3}$ = 2.363H + 0.226. These lines summarize trends in the cases and are not design or inversion equations.

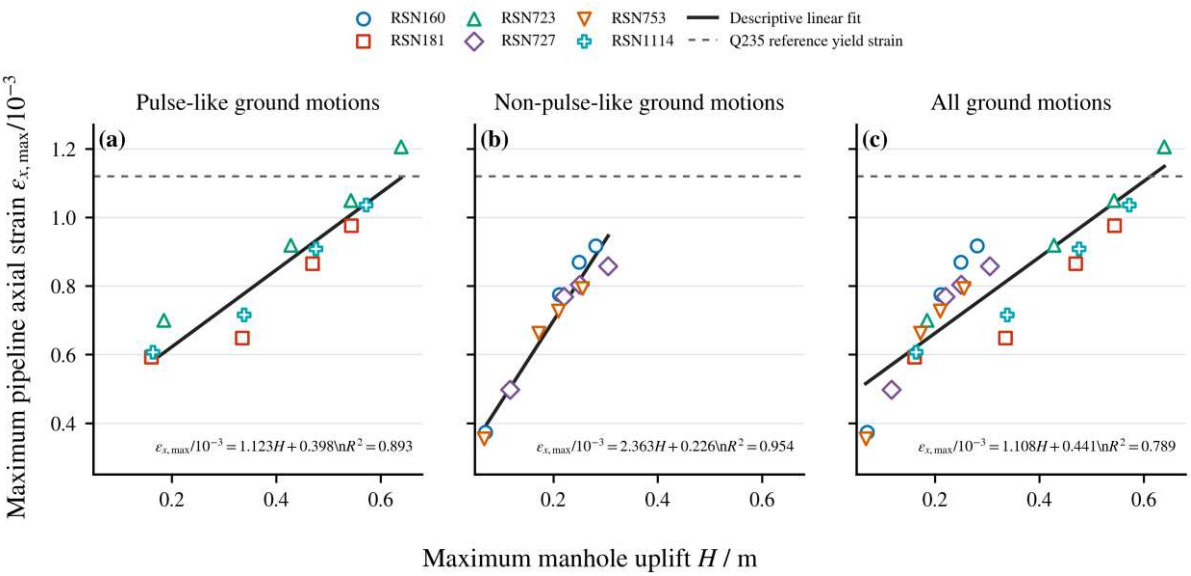


Fig. 16 Relationship between maximum manhole uplift and maximum pipeline axial strain with descriptive linear fits: (a) pulse-like motions; (b) non-pulse-like motions; (c) all motions

Because four PGA levels from a single record are not fully independent, sensitivity was evaluated by removing all four cases from one record at a time. The six leave-one-record-out Pearson coefficients ranged from 0.836 to 0.920 and remained strongly positive. The smallest coefficient occurred after removing RSN723, confirming that the high pulse-like response influenced the correlation magnitude. The coefficients and fitted lines should therefore be interpreted as descriptive evidence for these cases rather than population statistics or probabilistic engineering models. Over PGA = 0.1–0.4 g, all non-pulse-like cases remained below the Q235 reference strain; the RSN723 case at PGA = 0.4 g reached 0.639 m uplift and a maximum axial strain of 1.206×10^{-3}, becoming the first present case to exceed the reference value of 1.12×10^{-3}.

Both motion groups showed a positive internal association but different slopes and intercepts. H mainly reflects cumulative uplift of the manhole and neighboring pipe, whereas εx,max is further controlled by liquefied-zone boundaries, deformation compatibility at manhole-adjacent connections, degradation of pipe–soil restraint, and transient excitation. The defensible use of H is therefore relative risk classification and inspection priority, not direct back-calculation of actual strain or damage type.

4.2 Three-Level Inspection Zoning

Risk in this study means the relative inspection priority of a potentially abnormal structure under comparable consequence levels. It is not the product of failure probability and consequence and does not correspond to a code safety class. In the numerical analyses, H is the stable postshaking uplift plateau. As shown in Fig. 11, the responses generally reached stable plateaus late in the input, supporting use of this quantity to represent visible

postshaking uplift. In field use, H is measured as the height difference between the manhole top and the surrounding stable pavement, while surface cracking, sand boils, joint offset, leakage, abnormal pressure, and service condition are recorded concurrently. Measurements should avoid debris, repair layers, and obvious local settlement and should use multiple points around the manhole to obtain a representative relative height difference. Numerical plateau uplift and the field-measured relative height difference are not strictly identical; the zoning is therefore used only to allocate inspection resources and not to convert H directly into pipeline strain.

For the 0.8-m-outside-diameter pipe, burial depth, soil profile, connection, and selected motions examined here, $H = 0.30$ and 0.64 m are case-specific zoning references. $H < 0.30$ m is assigned to routine patrol; $0.30\ \text{m} \le H < 0.64$ m to review of joints, surface deformation, and service condition; and $H \ge 0.64$ m to priority inspection by specialized testing or excavation. The 0.64-m value is 0.639 m rounded to two decimal places and corresponds to the first present case above the Q235 reference strain. The 0.30-m value was selected as a practical zoning reference close to the upper end of the high-PGA non-pulse-like response, approximately 0.305 m. Neither value is a material-damage threshold or transferable code limit.

Fig. 17 relates field examples to the zoning logic. Manholes uplifted by 1.0–1.2 m during the Noto Peninsula earthquake [3]; Tohoku examples showed approximately 0.50 m of uplift and no visible uplift [2]. The photographs illustrate observable features but were not used to calibrate the boundaries. Leakage, abnormal pressure, through-cracks in pavement, or joint offset should trigger escalation even when H is small; a large H warrants higher priority even if the exterior appears intact. This visible-quantity screening, accompanying-anomaly correction, and specialized-confirmation sequence is consistent with progressive municipal-pipeline assessment [6, 23].

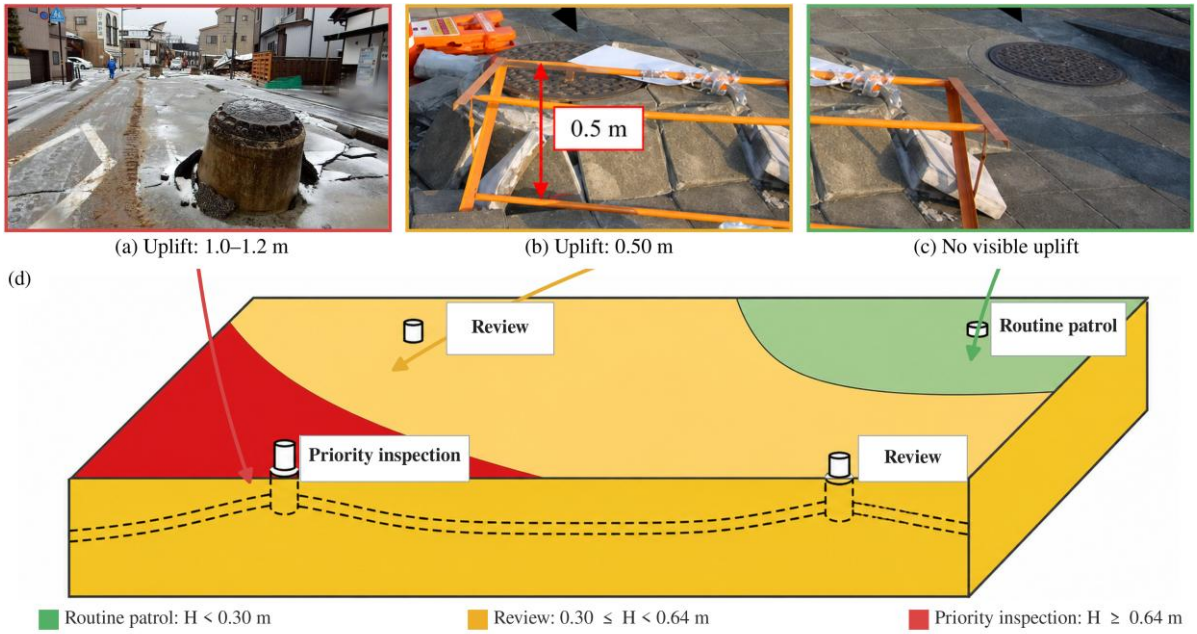


Fig. 17 Three-level post-earthquake inspection zoning based on manhole uplift with field cases: (a) priority-inspection case; (b) review case; (c) routine-patrol case; (d) three-level inspection zoning. Sources: (a) Ref. [3]; (b, c) Ref. [2]. Reproduced with permission.

5 Conclusions

1. To address concealed post-earthquake damage and the impracticality of immediate detailed coverage of all buried pipelines in liquefied ground, this study used manhole uplift H as an observable surface proxy and established a visible-uplift–internal-strain–inspection-priority screening chain. Risk denotes relative inspection priority, and H does not directly determine actual pipeline damage.

2. A coupled FLAC3D model that included pore-pressure accumulation, degradation of pipe–soil restraint, manhole–soil slip, and manhole–pipeline load transfer was validated against an approximately 0.50-m Tohoku manhole-uplift case. Calculated uplift was 0.553 m, differing by 10.6%, and the global heave pattern was reproduced. Because synchronous motion, local soil data, and field strain were unavailable, subsequent strains support relative case comparison rather than unique local-damage prediction.

3. In the selected sample, both H and $\varepsilon_{x,max}$ generally increased with PGA. At PGA = 0.4 g, the pulse-like mean uplift was 0.585 m, 2.1 times the non-pulse-like mean of 0.280 m; mean maximum strains were 1.073×10^{-3} and 0.856×10^{-3}. Pore-pressure growth generally preceded rapid uplift, and larger strains concentrated near liquefied–nonliquefied boundaries and manhole-adjacent connections. Across 24 cases, Pearson and Spearman coefficients were 0.888 and 0.883, and leave-one-record-out Pearson coefficients

were 0.836–0.920. H is reasonably robust for relative ranking, but different motion-group mappings preclude direct inversion of actual strain.

4. A three-level procedure was proposed using H with accompanying damage and service condition as correction information. Under the present 0.8-m pipe, burial, soil, connection, and motion conditions, H = 0.30 and 0.64 m are case-specific references between routine patrol, review, and priority inspection. The 0.64-m reference corresponds to the first present case above the Q235 reference strain, whereas 0.30 m is a practical zoning reference close to the upper end of the high-PGA non-pulse-like response. They are not universal damage thresholds. Leakage, abnormal pressure, through-cracks, or joint offset should directly escalate inspection; application to other pipelines requires recalibration for diameter, burial depth, soil structure, connection stiffness, and ground-motion characteristics.

Nomenclature

The following symbols are used in this paper:

D = pipeline outside diameter;

G = soil shear modulus;

H = stable postshaking manhole uplift;

Hf = final manhole uplift;

K = soil bulk modulus;

Mw = moment magnitude;

Rrup = shortest distance from the site to the rupture plane;

c = manhole–soil interface cohesion;

ft = manhole–soil interface tensile strength;

k = manhole–pipeline connection stiffness;

kn = normal stiffness of the manhole–soil interface;

ks = shear stiffness of the manhole–soil interface;

kx, ky = axial and tangential pipe–soil spring stiffnesses;

kz,l, kz,u = lower- and upper-half radial pipe–soil spring stiffnesses;

r = Pearson correlation coefficient;

ru = pore-pressure ratio;

ru,max = maximum pore-pressure ratio;

t_0 = time at which uplift reaches 5% of final uplift;

t_{50} = time at which uplift reaches 50% of final uplift;

t_{95} = time at which uplift reaches 95% of final uplift;

t_{ru50} = time at which pore-pressure ratio reaches $0.5r_{u,max}$;

t_{ru70} = time at which pore-pressure ratio reaches 0.7;

Δt_1–Δt_4 = stage durations defined in Fig. 9(b);

Δz_{min} = minimum zone dimension normal to the interface;

$\varepsilon_{x,max}$ = maximum absolute pipeline axial strain;

η_H = ratio of pulse-like to non-pulse-like mean uplift;

η_ε = ratio of pulse-like to non-pulse-like mean axial strain;

ρ = Spearman rank correlation coefficient;

φ = manhole–soil interface friction angle.

Statements and Declarations

Funding: This work was supported by the Science and Technology Research and Development Project of China Harbour Engineering Co., Ltd. (Grant No. 2026-ZGKJ-TDYF-12).

Competing interests: The authors declare that they have no competing financial or non-financial interests.

Author contributions: Kewu Zhang developed the methodology, performed the numerical analyses, prepared the figures, and drafted the manuscript. Jiasheng Jiang contributed to validation and data curation. Qingyun Xu contributed to resources and project administration. Bo Song supervised the work, contributed to conceptualization, and revised the manuscript. All authors read and approved the final manuscript.

Availability of data and materials: The original ground-motion records were obtained from the PEER NGA-West2 database (https://ngawest2.berkeley.edu/). The processed and scaled ground-motion records, numerical models, response data, and code supporting the findings of this study are available from the corresponding author upon reasonable request.

Ethics approval: Not applicable.

Consent to participate: Not applicable.

Consent for publication: Permission for reuse in both print and online formats has been obtained from the relevant copyright holders for all previously published field photographs cited in the figure captions. Consent for publication has also been obtained for any identifiable persons shown in these photographs, where required.

References

1. Ministry of Housing and Urban-Rural Development of the People's Republic of China (2025) China urban construction statistical yearbook (2013–2024) (in Chinese). https://www.mohurd.gov.cn/gongkai/fdzdgknr/sjfb/tjxx/jstjnj/index.html. Accessed 3 Feb 2026

2. Yamaguchi A, Mori T, Kazama M, Yoshida N (2012) Liquefaction in Tohoku district during the 2011 off the Pacific Coast of Tohoku Earthquake. Soils Found 52(5):811–829. https://doi.org/10.1016/j.sandf.2012.11.005

3. Shoji M, Miyajima M, Nojima N, Tobita T, Ono Y, Maruyama Y, Kuwata Y, Ishikawa K, Shumuta Y, Okutsu D (2025) Damage to lifelines caused by the 2024 Noto Peninsula earthquake (in Japanese). J Jpn Geotech Soc Disaster Surv Rep 3(1):20–40. https://doi.org/10.11512/jgsdr.3.1_20

4. Niigata Prefecture Department of Public Works (n.d.) Record of the Niigata-ken Chuetsu-oki Earthquake (in Japanese). https://www.pref.niigata.lg.jp/sec/dobokukanri/1255464221640.html. Accessed 9 Apr 2025

5. Ministry of Housing and Urban-Rural Development of the People's Republic of China (2017) Seismic technical code for oil and gas transmission pipeline engineering: GB/T 50470–2017 (in Chinese). China Planning Press, Beijing

6. China Association for Engineering Construction Standardization (2022) Standard for structural safety risk assessment of urban municipal pipelines: T/CECS 1120–2022 (in Chinese). China Architecture & Building Press, Beijing

7. Yasuda S, Kiku H (2006) Uplift of sewage manholes and pipes during the 2004 Niigataken-Chuetsu earthquake. Soils Found 46(6):885–894. https://doi.org/10.3208/sandf.46.885

8. Kang GC, Tobita T, Iai S (2013) Damage to sewerage systems during the 2004 earthquake in Niigata-ken Chuetsu, Japan. Eng Geol 164:230–242. https://doi.org/10.1016/j.enggeo.2013.07.011

9. Koseki J, Matsuo O, Sasaki T, Saito K, Yamashita M (2000) Damage to sewer pipes during the 1993 Kushiro-Oki and the 1994 Hokkaido-Toho-Oki earthquakes. Soils Found 40(1):99–111. https://doi.org/10.3208/sandf.40.99

10. Nishio N, Tsukamoto K, Hamura J (1987) Model experiment on the seismic behavior of buried pipeline in partially liquefied ground (in Japanese). Proc Jpn Soc Civ Eng 1987(380):449–458. https://doi.org/10.2208/jscej.1987.380_449

11. Ko YY, Tsai TY, Jheng KY (2023) Full-scale shaking table tests on soil liquefaction-induced uplift of buried pipelines for buildings. Earthq Eng Struct Dyn 52(5):1486–1510. https://doi.org/10.1002/eqe.3834

12. Tobita T, Kang GC, Iai S (2011) Centrifuge modeling on manhole uplift in a liquefied trench. Soils Found 51(6):1091–1102. https://doi.org/10.3208/sandf.51.1091

13. Lin J, Xiong J (2000) Analysis for floating response of buried pipeline in liquefied soil (in Chinese). Earthq Eng Eng Dyn 20(2):97–100. https://doi.org/10.3969/j.issn.1000-1301.2000.02.016

14. Valizadeh H, Ecemis N (2022) Soil liquefaction-induced uplift of buried pipes in sand-granulated-rubber mixture: numerical modeling. Transp Geotech 33:100719. https://doi.org/10.1016/j.trgeo.2022.100719

15. Chen Y, Li L, Li D, Yang M (2016) Influence factor analysis of floatation response of buried pipeline in liquefied soil (in Chinese). World Earthq Eng 32(4):182–187

16. Basu D, Wijewickreme D (2024) Influence of ground motion characteristics on liquefaction-induced pipe uplift. Jpn Geotech Soc Spec Publ 10(22):838–842. https://doi.org/10.3208/jgssp.v10.OS-11-06

17. Mardonov B, Mirzaev I, Nishonov N, An E, Kosimov E (2024) Study of the uplift of buried pipelines in liquefied soils based on the earthquake record. E3S Web Conf 515:04009. https://doi.org/10.1051/e3sconf/202451504009

18. Hu J, Pang L (2023) Identifying the optimal intensity measure and key factors of earthquake liquefaction-induced uplift of underground structures. Bull Eng Geol Environ 82:31. https://doi.org/10.1007/s10064-022-03043-y

19. Nakao K, Yamaguchi H, Hoshino S, Inazumi S (2022) Applicability of weighting method as measure for existing manholes against uplifting during liquefaction. Appl Sci 12(8):3818. https://doi.org/10.3390/app12083818

20. Tobita T, Kang GC, Iai S (2012) Estimation of liquefaction-induced manhole uplift displacements and trench-backfill settlements. J Geotech Geoenviron Eng 138(4):491–499. https://doi.org/10.1061/(ASCE)GT.1943-5606.0000615

21. Zhang Z, Chian SC (2022) Revisiting factor of safety used for manhole uplift induced by soil liquefaction. Acta Geotech 17:441–452. https://doi.org/10.1007/s11440-021-01237-2

22. Lu CW, Lin YF, Lee WL (2024) An analytical model for liquefaction-induced manhole uplifting. Soil Dyn Earthq Eng 180:108562. https://doi.org/10.1016/j.soildyn.2024.108562

23. Jing H, Huang L, Du Y, Niu R, Deng Q (2025) Preliminary construction of a rapid safety assessment framework for long-distance oil and gas pipelines after earthquakes (in Chinese). Saf Environ Eng 32(6):82–93. https://doi.org/10.13578/j.cnki.issn.1671-1556.20250319

24. Shahi SK, Baker JW (2014) An efficient algorithm to identify strong-velocity pulses in multicomponent ground motions. Bull Seismol Soc Am 104(5):2456–2466. https://doi.org/10.1785/0120130191

25. Takada S (1988) Liquefaction analysis of underground pipelines. In: O'Rourke TD, Hamada M (eds) Seismic resistance of underground pipelines. Academic Press, Orlando, pp 59–71